ROYAL SOCIETY OPEN SCIENCE

royalsocietypublishing.org/rsos

Research

Cite this article: Svirskaite LM, Kamarauskas E, Jegorove A, Getautis V, Malinauskas T, Jankauskas V, Čepas RJ, Gruodis A, Genevičius K. 2026 Cross-linkable naphthalene diimide acceptors for applications in photovoltaic devices. *R. Soc. Open Sci.* **13**: 251725.
https://doi.org/10.1098/rsos.251725

Received: 11 September 2025
Accepted: 20 April 2026

Subject Category:
Physics and biophysics

Subject Areas:
chemical physics

Keywords:
n-type semiconductors, cross-linking polymerization, naphthalene diimide, charge carriers transport, photovoltaics

Author for correspondence:
Egidijus Kamarauskas
e-mail: egidijus.kamarauskas@ff.vu.lt

Supplementary material is available online at https://doi.org/10.6084/m9.figshare.c.8449374.

THE ROYAL SOCIETY PUBLISHING

Cross-linkable naphthalene diimide acceptors for applications in photovoltaic devices

Lauryna M. Svirskaite[1], Egidijus Kamarauskas[2], Aiste Jegorove[1], Vytautas Getautis[1], Tadas Malinauskas[1], Vygintas Jankauskas[2], Romualdas J. Čepas[2], Alytis Gruodis[2] and Kristijonas Genevičius[2]

[1]Department of Organic Chemistry, Kaunas University of Technology, Kaunas, Lithuania
[2]Institute of Chemical Physics, Vilnius University, Vilnius, Lithuania

EK, 0000-0002-4818-7105

Cross-linkable naphthalene diimide (NDI) electron-transporting materials (ETMs) bearing vinylbenzyl groups were designed, synthesized and evaluated for possible photovoltaic applications. A one-pot condensation followed by *O*-alkylation reaction was employed to synthesize new compounds. The new NDIs are sufficiently thermally and electrochemically stable owing to the presence of vinyl groups; all compounds are able to undergo thermal cross-linking by heating at 199°C and 213°C. Differential scanning calorimetry (DSC) and solubility tests revealed a two-step cross-linking mechanism: a low-temperature linear polymerization followed by high-temperature three-dimensional network formation. Cross-linking causes minimal changes in electron mobility in neat films, but in donor–acceptor blends it increases electron mobility by a factor of approximately 2–3, maintains stable hole transport, suppresses deep-trap formation and stabilizes quantum efficiency of photogeneration over time. These results establish vinylbenzyl-functionalized NDIs as promising, solution-processable n-type semiconductors for solvent-resistant, thermally robust electron-transport layers for perovskite or organic photovoltaics.

1. Introduction

The field of cross-linked charge transporting materials is rapidly expanding in the applications wherever low-temperature fabrication, flexibility, semi-transparency or light weight are desirable [1]. The thermal cross-linking process has been widely utilized in recent years, especially with small molecule semiconductors containing cross-linkable functional fragments, such as vinyl units [2]. Cross-linking process can adjust or significantly change the functionality of semiconductors: the polymers attain specific morphological, optical and electrical properties [3]. The advantages of cross-linked charge transporting materials include good resistance to solvents, high thermal stability and excellent film-forming properties, overcoming the morphological instabilities often seen with small molecules [1,2]. Furthermore, cross-linking can influence the distance among molecules, rearrange them geometrically and thus affect the width of the energy state distribution and the spatial disorder thereby affecting charge transport and photo adjacent layers [4].

Charge transport studies of the cross-linked materials mainly cover the design and investigation of hole transporting materials (HTMs) for uses in perovskite photovoltaic technology [5]. As an example, Wang *et al.* proposed an *in situ* cross-linked N_4,N_4′-di(naphthalen-1-yl)-N_4,N_4′-bis(4-vinylphenyl)biphenyl-4,4′-diamine (VNPB) as an HTM to replace the commonly used poly[bis(4-phenyl)(2,4,6-trimethylphenyl)amine] (PTAA) in tandem solar cells [6]. The strong interaction and lower defect density at the HTM/perovskite interface resulted in improved efficiency of 15.9% and stability of wide bandgap perovskite solar cells compared to control devices (15%). Moreover, *in situ* cross-linked VNPB reached better power conversion efficiency with tandem solar cells, where absorbers of perovskite/perovskite and perovskite/silicon achieved an efficiency of 24.9% and 25.4%, respectively [6]. A variety of different thermally cross-linkable semiconductors has been published by the V. Getautis research group. In all cases, the photovoltaic performance of perovskite-devices demonstrated high operational stability, better V_{OC} along with increased power conversion efficiency compared to perovskite solar cells using conventional p-type semiconductors [7–11]. Note that all aforementioned results show that cross-linkable HTMs benefit the long-term stability of perovskite solar cells making them very attractive for possible commercial applications. In bulk heterojunction photovoltaics, cross-linking stabilizes the nanoscale donor–acceptor morphology—critical for efficient exciton dissociation, charge transport and long-term operation [12–14]. This approach also holds promise for ternary A–D–chromophore blends, where morphology control remains key to further efficiency gains [15]. Despite these advances, cross-linkable n-type semiconductors with vinyl groups remain largely unexplored for perovskite solar cell applications. Over the past decade, research on naphthalene and perylene diimide copolymers incorporating vinylene, bithiophene imide, dibenzosilole, thiophene, selenophene and related motifs has yielded only modest photovoltaic performance, often with complex synthetic routes [16–18]. Motivated by the success of cross-linkable HTMs and the lack of efficient n-type analogues, we have designed, synthesized and investigated new vinylbenzyl-functionalized naphthalene diimide (NDI) derivatives. Incorporation of di-*tert*-butylphenyl and pentafluorophenyl fragments into the chromophore enhanced solubility and hydrophobicity, thereby improving device stability by inhibiting moisture ingression. These compounds combine cross-linking capability with relatively straightforward synthesis, making them promising electron-transporting materials (ETMs) for photovoltaic devices. The structures used in this study are presented in figure 1.

2. Results and discussion

The semiconductors *V1525*, *V1547* and *V1560* were synthesized according to synthesis procedures described in the electronic supplementary material. The synthesis of the NDI intermediates **1**–**3** was done by implementing a one-pot reaction concept [19]. One-pot synthesis is carried sequentially by adding equivalent molar ratios of the appropriate amines (1 : 1 : 1.2) into the reaction mixture without separating the intermediate products. The initial step was condensation of the 1,4,5,8-naphthalenetetracarboxylic dianhydride with 5-aminoresorcinol or 4-aminoresorcinol hydrochloride in anhydrous dimethylformamide (DMF) at 140°C for 6–24 h under argon atmosphere (scheme 1). Thereafter, 2,5-di-*tert*-butylaniline or 2,3,4,5,6-pentafluoroaniline were added, and the reaction mixture was refluxed for additional 8–12 h, yielding corresponding intermediates **1**–**3**. Finally, NDIs **1** and **2** were used for the *O*-alkylation reaction with 4-(chloromethyl)styrene using K_2CO_3 and KI in anhydrous DMF at room temperature isolating NDI with vinylbenzyl moiety as a reactive group enabling thermal polymerization. For *V1560*, KI was omitted and the reaction was carried out at 50°C. The

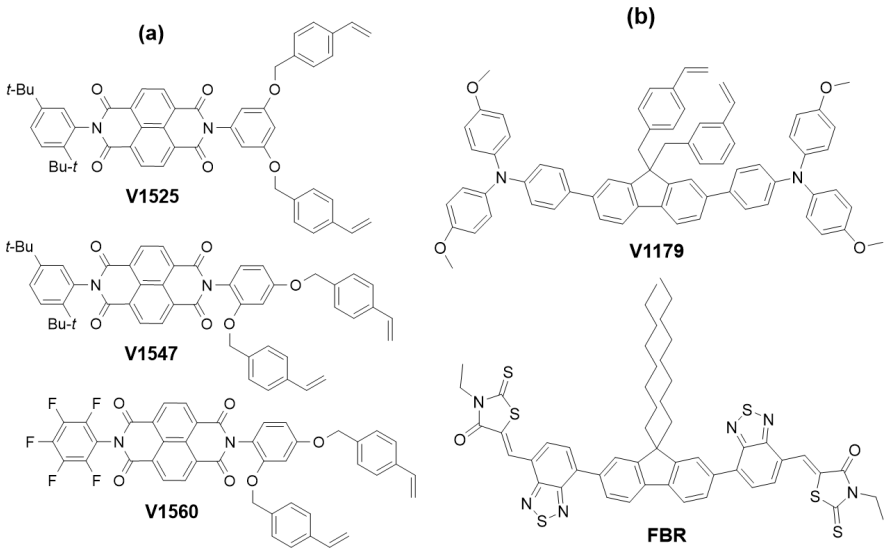

Figure 1. Cross-linkable NDIs *V1525*, *V1525* and *V1560* (a) and structures of *V1179* and *FBR* used in this study (b).

molecular structure of compounds was confirmed by nuclear magnetic resonance analysis, as shown in electronic supplementary material, figs. S1–S10.

UV–Vis spectra (figure 2a) in tetrahydrofuran (THF) revealed three characteristic π–π* absorption bands (330–385 nm) for the NDI chromophore. Optical bandgaps E_g^{opt} were approximately 3.17–3.18 eV for all compounds (table 1). Cyclic voltammetry was employed to give insight into the electrochemical stability and to determine the E_{LUMO} and E_{HOMO} energy levels of synthesized ETMs. These values do not represent any absolute solid-state electron affinity, but can actually be used to compare different compounds in relation to one another. Voltammograms (figure 2b) showed two quasi-reversible reduction waves, which is typical for NDI derivatives. The reversible process indicates that all ETMs exhibit good electrochemical stability, with the formation of stable anion radicals during the scans.

E_{LUMO} values (approx. −4.11 to −4.26 eV) are well-matched with conduction bands of common absorbers such as perovskites (approx. −4.0 eV) and Sb_2Se_3 (approx. −4.15 eV), while E_{HOMO} levels (less than −7.0 eV) effectively block hole leakage.

The thermal decomposition and thermal polymerization of the synthesized NDIs were investigated by thermogravimetric analysis (TGA) and differential scanning calorimetry (DSC). NDIs *V1525*, *V1547* and *V1560* demonstrated weight loss of 5% at 403°C, 398°C and 359°C, respectively (figure 3a). When comparing structurally similar ETMs *V1525* and *V1547*, the change of the position of [(4-vinylbenzyl)oxy] fragment from 3,5- to 2,4- in the phenyl ring has a slight effect on the thermal decomposition: TGA curves show that thermal degradation temperature decreases by 5°C. These results confirm that the symmetrical positioning of the fragments in materials structure determines the retention for high thermal stability. Note that lower thermal stability of *V1560* probably arises from fluorine substitution. Overall, it is evident that all NDIs are sufficiently thermally stable for their prospective applicability in photovoltaic devices.

According to the DSC measurements, during the first heating the glass transition temperatures were recorded at 91°C, 74°C and 82°C for diimides *V1525*, *V1547* and *V1560*, respectively (figure 3b–d). Subsequently, the melting points and exothermic peaks were identified at 203°C, 187°C and 213°C, 199°C for compounds *V1547*, *V1560*, accordingly. The DSC results indicate that NDI monomers exist as a mixture of amorphous and crystalline states. These compounds first undergo melting of the crystals and then thermal polymerization. For the NDI *V1525* only exothermic process was observed at 213°C during the first heating step, indicating that material is fully amorphous and only the thermal polymerization step is observed. No peaks related to crystallization and glass transition were detected for all synthesized NDI monomers during the cooling and second heating cycles, suggesting a formation of the polymers.

Cross-linking conversion efficiency and resistance to a solvent of cross-linked films were also tested. Cross-linking films were dipped into THF for 15 min and UV–Vis spectra were recorded to evaluate the amount of the washed ETMs (electronic supplementary material, fig. S12). Cross-linking longer than 1 h does not decrease solubility of ETM further. Absorption maximum at longer wavelengths are reduced by 1.5 times only, but duration of immersion is very long, so cross-linked layers are resistant enough to form other layers on top.

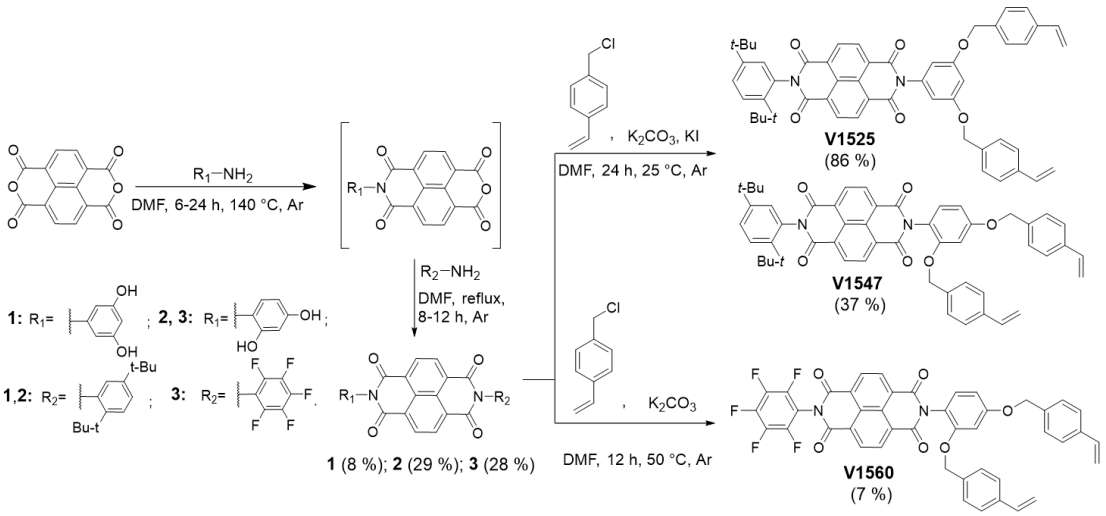

Scheme 1. Synthetic route for NDIs *V1525*, *V1547* and *V1560* containing vinyl benzyl moieties.

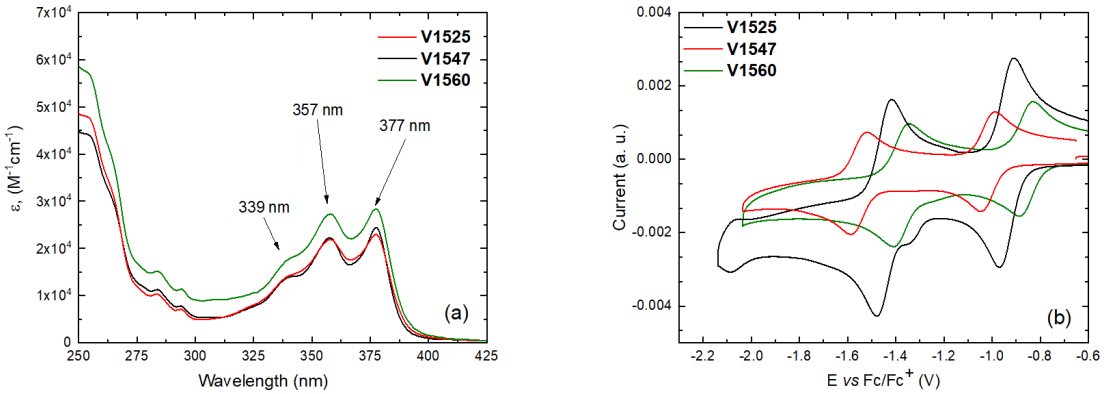

Figure 2. UV–Vis spectra of *V1525, V1547* and *V1560* in THF solution ($c = 10^{-4}$ M) (a) and redox voltammograms of the investigated compounds (b).

Table 1. Energy level values for *V1525*, *V1547* and *V1560*.

ETM	[a]E versus Fc/Fc+ [V]	[b]E_{LUMO} [eV]	[c]E_{HOMO} [eV]	$\lambda_{a.e}$ [nm]	[d]Egopt [eV]
V1525	−0.95	−4.17	−7.35	389	3.18
V1547	−1.01	−4.11	−7.28	390	3.17
V1560	−0.86	−4.26	−7.43	391	3.17

The cyclic voltammetry measurements were carried out at a glassy carbon electrode in DMF solutions containing 0.1 M tetrabutylammonium hexafluorophosphate as an electrolyte, Pt as the counter electrode and as the reference electrode.

[a]Each measurement was calibrated with ferrocene (Fc), and the potentials were calculated to Fc^+/Fc.

[b]Conversion factors: ferrocene in DMF versus SCE: 0.45, SCE versus SHE: 0.244, SHE versus vacuum: 4.43 [20,21].

[c]E_{HOMO} was calculated from the equation $E_{HOMO} = E_{LUMO} - E_g^{opt}$.

[d]Optical band gaps E_g^{opt} estimated from the edges of UV–Vis spectra in solution.

During the cross-linking of NDI monomers, changes in the UV–Vis absorption spectra occur (figure 4). The absorption region in the 330–385 nm range, for which the NDI chromophore is responsible, remains practically unchanged after cross-linking. In addition, the absorption owing to the conjugated system between the phenyl and vinyl groups in the 250–260 nm region decreases noticeably. During cross-linking the vinyl groups react, the conjugated system decreases and the absorption intensity in this region decreases. Similar changes in the 250 nm maximum were observed for other NDI derivatives (electronic supplementary material, fig. S11) in the thin layers cross-linking experiment (electronic supplementary material, fig. S12).

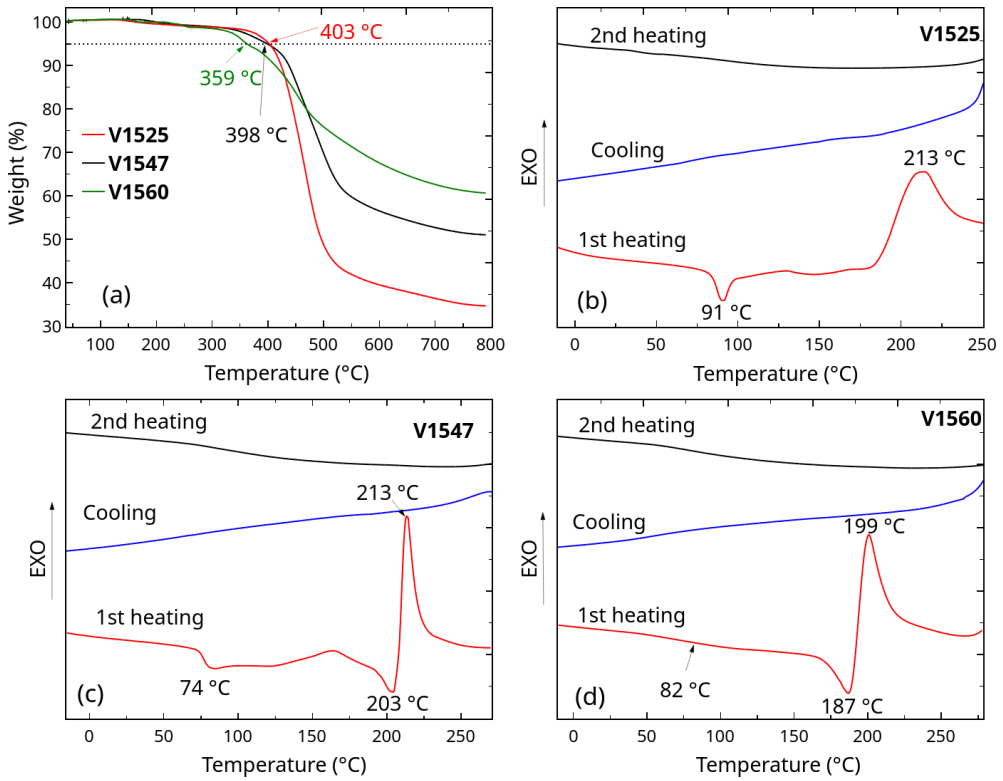

Figure 3. TGA (a) and DSC curves of cross-linkable ETMs *V1525*, *V1547* and *V1560* (b, c and d).

Xerographic time-of-flight (XTOF) measurements were employed to investigate the charge transport properties of the synthesized NDI derivatives. The measurements were carried out in thin films obtained by drop-casting THF solutions of NDI's (10 mg ml^{-1}) on to glass substrates coated with an evaporated Al layer. Figure S14a,c,e in electronic supplementary material shows representative dU/dt electron transients profiles for the thin film of *V1525*, *V1547* and *V1560*. The materials exhibit dispersive electron transport, accompanied by a strong dependence of mobility on the applied electric field—indicative of trap-limited transport behaviour. The field dependence of electron mobilities for given NDI is presented in figure 5a. In all cases investigated mobility μ follows Pool–Frenkel type field dependence: $\mu = \mu_0 exp(\alpha\sqrt{E})$, here μ_0 is the zero-field mobility, α is field dependence parameter and E is electric field strength. The extracted mobility parameters μ_0 and α, as well as the mobility values at an electric field of 1×10^5 V cm^{-1}, are listed in table 2.

During cross-linking, the formation of additional chemical bonds may alter the arrangement of molecules within the layer, which in turn can lead to changes in charge carrier mobility. In our case, only minor variations in electron drift mobility were observed, suggesting that the molecular rearrangements induced by cross-linking are minimal (figure 5b). Although *V1560* exhibited somewhat higher mobilities, its XTOF kinetics were more dispersive, and transit times were observed only at higher applied voltages compared to *V1525* and *V1547* (electronic supplementary material, fig. S14b,d,f).

The spatial arrangement of reactive groups can be adjusted not only by modifying the molecular structure but also by blending the material with other compounds. This approach enables the formation of donor–acceptor systems that are resistant not only to solvents but also to environmental oxidation. *V1525* was selected for blend studies because of its stable mobility upon cross-linking and relatively low trap density compared to *V1547* and *V1560*. V1179 [22] was employed as the hole-transporting donor material (electronic supplementary material, fig. S15), as its molecular structure—based on modelling—was expected to promote the formation of a fully cross-linked three-dimensional network.

As expected, in the *V1179* + *V1525* blend (1 : 1 mass ratio), a reduction in both electron and hole mobilities was observed compared to the pure materials. However, after cross-linking, electron mobility increased by a factor of 2–3, while hole mobility remained nearly unchanged (figure 6a). To evaluate the V1179 + V1525 system in the presence of a chromophore, the well-known small-molecule compound FBR [23] was used. FBR is known for its excellent compatibility with a wide range of

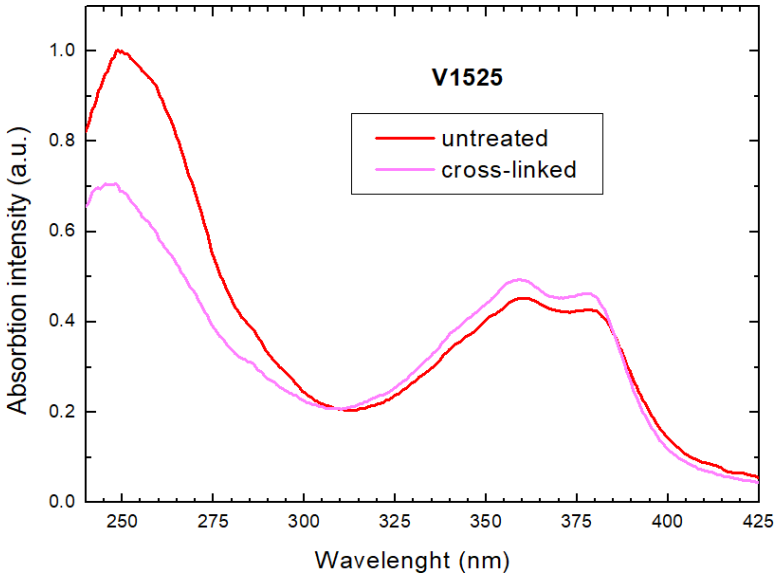

Figure 4. UV–Vis spectra of *V1525* thin layer before heating and after cross-linking at 215 °C for 1 h in glovebox.

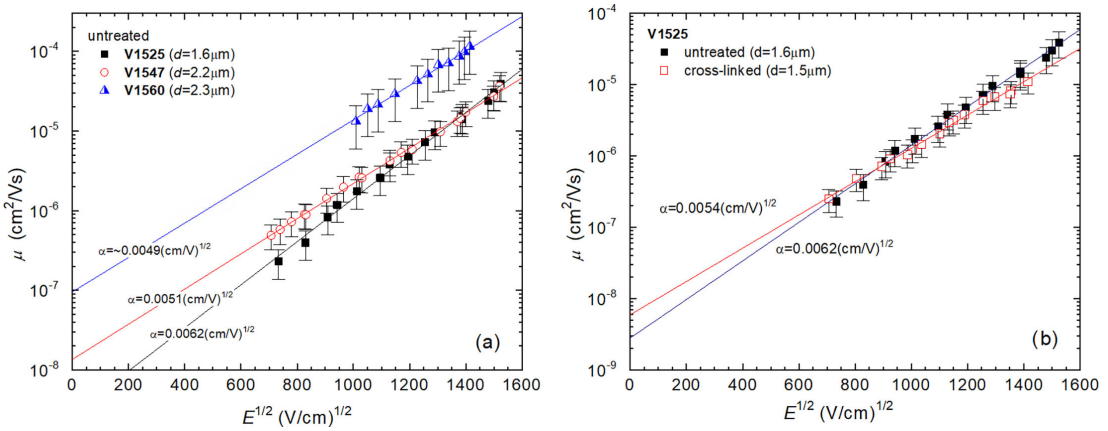

Figure 5. Electric field dependencies of the electron drift mobility in untreated films of V1525, *V1547*, *V1560* (a) and in untreated and cross-linked films of *V1525* (b).

Table 2. Electron drift mobility data in untreated and cross-linked films *V1525*, *V1547* and *V1560* compounds.

Sample	*d*, μm	μ_0, $cm^2\ Vs^{-1}$	μ (10^6 V cm^{-1}), $cm^2\ Vs^{-1}$	α $(cm\ V^{-1})^{1/2}$
V1525	1.6	3×10^{-9}	1.4×10^{-6}	0.0062
V1525 cross-linked	1.5	6×10^{-9}	1.3×10^{-6}	0.0054
V1547	2.2	1.4×10^{-8}	2.2×10^{-6}	0.0051
V1547 cross-linked	1.2	0.8×10^{-8}	2.2×10^{-6}	0.0056
V1560	2.3	-1×10^{-7}	1.3×10^{-5}	−0.005
V1560 cross-linked	2.2	1.2×10^{-8}	8×10^{-6}	~0.0066

organic materials, often forming amorphous glassy composites. The formed *V1525* + *V1179* + FBR (1 : 1 : 1 mass ratio) blend is characterized by hole and electron transport with clearly distinguishable flight times (electronic supplementary material, fig. S16). After cross-linking, hole and electron mobilities decreased similarly to those observed in the *V1179* + *V1525* mixture. No further changes in mobility values were observed over time for either untreated or cross-linked samples. However, in the untreated sample, the formation of deep traps was detected over time, as evidenced by a shift in the minimal field at which a transit time could be observed, in contrast to the cross-linked sample (figure 6b).

The quantum efficiency of photogeneration in the cross-linked layer changes very little over time (electronic supplementary material, fig. S17b). Initially, it is slightly lower compared to the

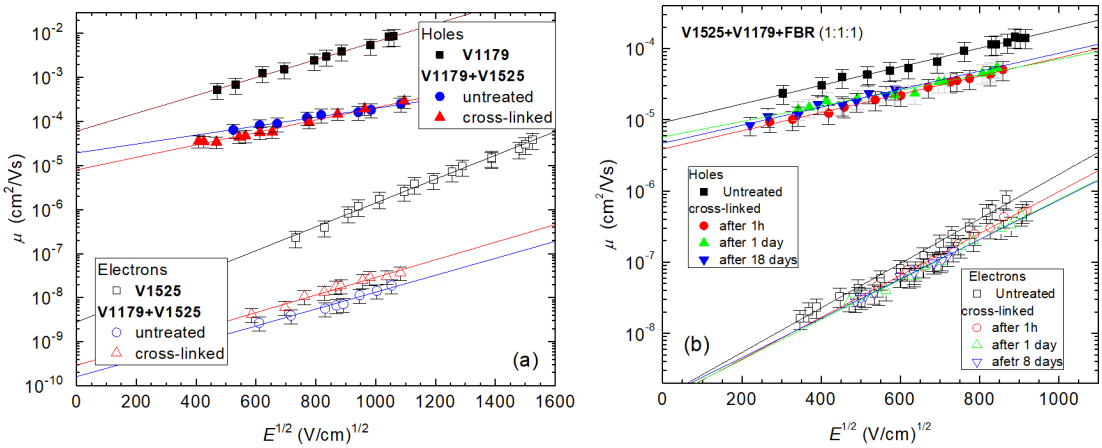

Figure 6. Electric field dependencies of the hole and electron drift mobility in pure *V1525*, *V1179*, untreated mixture of *V1179* + *V1525* and cross-linked mixture of *V1179* + *V1525* (a) and in films of *V1179* + *V1525* + *FBR (1:1:1)* (b) Cross-linking was performed at 200°C for 1 h in glovebox.

non-cross-linked sample (electronic supplementary material, fig. S17a), but it remains stable throughout the entire observation period as the sample ages (22–23°C, 35–45% humidity in the dark) (figure 7). In contrast, the untreated sample performance degrades quite fast over time, after a few weeks, the photogeneration efficiency drops by two orders of magnitude at weak electric fields, and by an order at strong fields during the observation period.

To clarify the nature of the cross-linking process, DSC measurements were performed on the blend, along with film solubility tests. The DSC thermograms of the *V1525+V1179+FBR* mixture (figure 8) reveal two exothermic peaks at 148.88°C and 226.48°C. Solubility testing (electronic supplementary information) indicated that the first exothermic peak corresponds to polymerization that does not provide sufficient resistance to THF, suggesting that this process produces linear polymerization. This exothermic reaction probably involves a single styrene branch of a *V1179* and/or *V1525* molecule. It is believed that the second styrene branches are sterically hindered or unfavourably oriented, and can participate in polymerization only at higher temperatures. The solubility experiment (electronic supplementary material, fig. S13) supports this assumption, showing that films polymerized at higher temperatures are significantly more resistant to solvent exposure, confirming the occurrence of three-dimensional network formation, i.e. cross-linking. In addition, the inflection observed in the second heating curve around 172°C could be attributed to the glass transition temperature of the FBR fraction in cross-linked media.

Molecular structure optimization and corresponding simulation of electronic excitations have been made using the Gaussian16 [24] package. Structure optimization at the ground electronic state has been performed at the density functional theory (DFT) level using the semi-empirical CAM-B3LYP method and the 6-31G(d) basis set, which includes polarization functions (d). Electronic excitations were calculated using the semi-empirical time-dependent method for singlets only. Environmental solvation effects were not included. The list of simulated monomers is listed in table 3. Table 4 lists HOMO–LUMO levels of monomers using the semi-empirical CAM-B3LYP method.

After successful optimization of monomer structure using the DFT method (table 4), it is possible to conclude that the HOMO level is placed at approximately the same position in the energetic scale (−7.3 ± 0.1) eV for all three monomers M1, M2 and M3. For estimating the gap between LUMO and HOMO, the largest value of 5.18 eV for M1, the intermediate value of 5.14 eV for M2, and the smallest value of 4.99 eV for M3 weakly correlate with the experimental values listed in table 1 (M1 and M2 only).

The properties of *V1525* (M1), *V1547* (M2) and *V1560* (M3) were numerically modelled and are described in detail in the electronic supplementary information. For *V1525*, the perpendicular orientation of its molecular fragments suggests a tendency toward ordered layering, potentially leading to crystallization within primitive p-type cells. In contrast, the non-perpendicular orientation in *V1560* favours the formation of amorphous, disordered structures, which is in good agreement with DSC results (figure 3b,c,d). The low-energy experimental bands at 377 nm and 357 nm (see figure 2) can be attributed to partially allowed transitions of the 'spectroscopic' states, corresponding to simulated wavelengths of 333 nm and 325 nm for *V1525*, 361 nm and 328 nm for *V1547*, and 375 nm and 327 nm for *V1560* (electronic supplementary material, tables S2 and S3). The observed

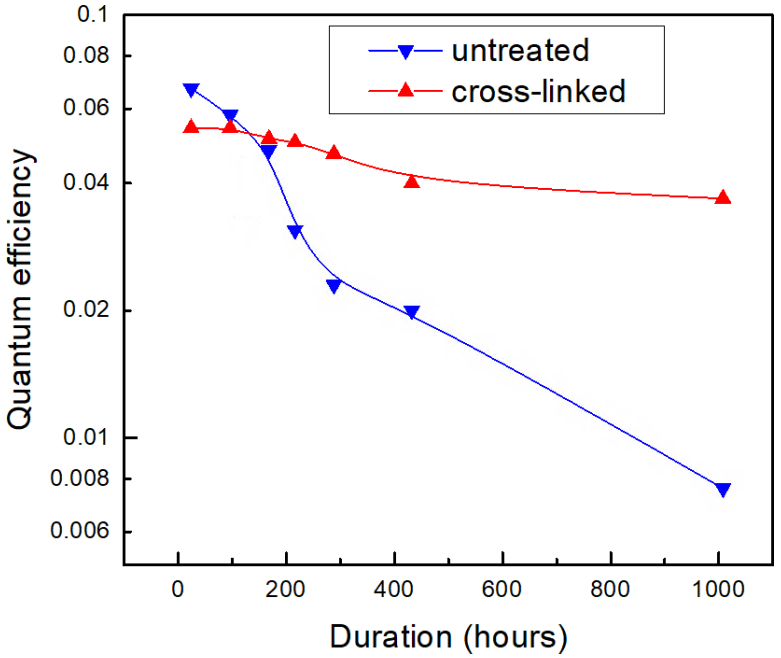

Figure 7. The photogeneration quantum efficiency dependences on ageing duration of *V1525* + *V1179* + *FBR* (1 : 1 : 1) untreated sample and cross-linked after ageing (cross-linking was performed at 200°C for 1 h) at $E = 5 \times 10^5$ V cm^{-1}.

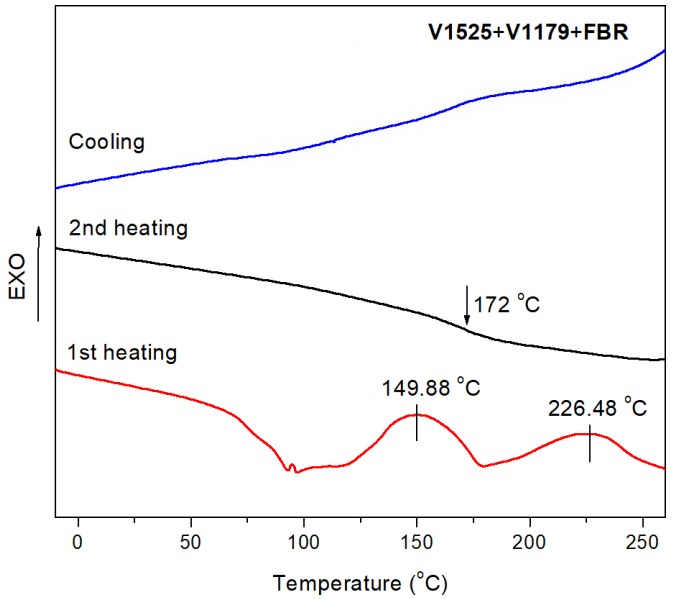

Figure 8. DSC curves of cross-linkable composition *V1525* + *V1179* + *FBR*.

Table 3. List of monomers.

abbreviation	chemical name and description	figure
M1	*V1525*	S17
M2	*V1547*	S17
M3	*V1560*	S18
M41	*V1179a*, first conformer, phenyl substituents oriented as butterfly-wings	S19
M42	*V1179b*, second conformer, phenyl substituents oriented quasi-linear	S19
M5	FBR	S18

Table 4. HOMO–LUMO levels (in eV) of monomers.

level	M1-V1525	M2-V1547	M3-V1560
LUMO+1	−0.29	−0.16	−0.46
LUMO	−2.24	−2.09	−2.32
HOMO	−7.42	−7.23	−7.31
HOMO-1	−7.44	−7.51	−7.56

discrepancies between experimental and calculated values—up to 0.5 eV—are typical for such semi-empirical time-dependent (singlet) calculations without solvation effects. The hypsochromic shift toward higher energies (shorter wavelengths) supports only qualitative assignment of the excitations, without precise energy-scale identification. According to electronic supplementary material, table S1, which lists the parameters of the six lowest excited states of the monomers M1, M2, M3, M41, M42 and M5, the hypsochromic shift is characteristic of all structures. In all cases, the estimation of the possible electronic activity is strongly related to the processes of molecular charge redistribution, and quantum chemical modelling allows the assessment of atypical donor–acceptor intra- and intra-molecular interactions. Figure 9 represents characteristic charge redistribution process along the long axis between bridged phenyl and core fragments.

To estimate the role of *V1179* and FBR (table 5) in the processes of cross-linking, three significant models are present. All models express non-covalent associates, where core-to-core realizations were done.

Electronic supplementary material, figs. S27 and S28 represent the following derivatives: (i) A32 = M1+M5 = V1525+FBR, (ii) A41 = M41+M5 = V1179a+FBR and (iii) A42 = M42+M5 = V1179b+FBR. In all cases, it is necessary to point out that two long tails of [–CH_2–] type play the role of barrier to separate the left- and right-hand part. Association motion could be realized at one of the left- as well as right-hand side only. Edge overlap of fragments (but not plane surface overlap) is typical for such type of associates. For A42, ordered orientation could be realized owing to successful 30° orientation of fragments—see electronic supplementary material, fig. S28, xz projection. Since a herringbone-like intramolecular structure forms on the left-hand side, which facilitates chaotic orientation, it can be assumed that the cross-linking process would begin at a lower temperature compared to other, purely chaotic structures. This structure of A42 is unique, as only the left-hand side of the structure tends towards an ordered packing orientation, while the right-hand side is oriented chaotically—see electronic supplementary material, fig. S28. In pure materials, linear cross-linking is dominant as a composite process, as it is a symbiosis of two opposing actions. First, each molecule has its own dipole moment, which usually coincides with or is oriented in the direction of the main axis of the core molecule. The parallel or antiparallel orientation (0° or 180°) of the dipole moments of both molecules (or their strongest components) determines the linear cross-linking as a process. In this case, the arrangement of the substituents in the perpendicular direction has little effect on the orientation of the dipoles. Second, at the macroscale, very close packing and rare packing are observed in such amorphous structures. The close packing structure is usually a physical dimer of the core-to-core type. In this case, the molecules are tightly bound, and there is no possibility of rearrangement. In low-density packings, owing to the prevailing chaos, the intermolecular bonds are organized randomly, because of jumping over the energy barrier. In this case, when two different molecules come into contact, there is no dipole orientation factor, which was essential in the first case. In this case, linear cross-linking is absent, and spatial cross-linking occurs owing to chaos arrangement. Structures A12 (electronic supplementary material, fig. S25), A22 (electronic supplementary material, fig. S26), A32(electronic supplementary material, fig. S27) and A42 (electronic supplementary material, fig. S28) represent low-density packing, where core-to-core orientation is absent, and only partial alignment is possible (especially for A32). Three factors are very important for describing the behaviour of composites. The possibility of flexible orientation of non-core substituents means that a large number of different conformers of low energy and closest-to-low energy exist (first factor). Second factor is a presence of pi-conjugated systems in substituents and those pi-conjugated systems interact with core system of composites. The orientation of the additional substituents is close to the perpendicular direction, which prohibits orientation along the optical axis, but allows a close to perpendicular orientation, which is energetically worse (especially FBR molecule, C8 chain). Owing to these three factors, three-dimensional cross-linking is more effective, especially since tight packing requires favourable conditions. In

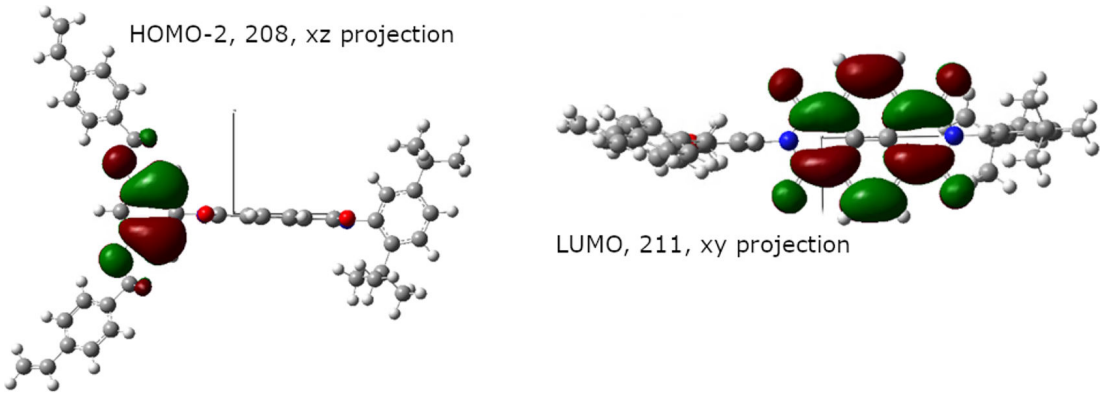

Figure 9. Monomer *V1525* (M1): hybrid molecular orbitals, which are involved (208 ⟶ 211) into first allowed spectroscopic transition S0⟶S1, see electronic supplementary material, table S2 and fig. S21.

Table 5. List of associates.

abbreviation	chemical name and description	figure
A11	M1 + M41 = V1525 + V1179a, non-covalent associate, core-to-core	S25
A12	M1 + M41 = V1525 + V1179a, monomer, tail-to-tail	S25
A21	M1 + M42 = V1525+V1179b, non-covalent associate, core-to-core	S26
A22	M1 + M42 = V1525 + V1179b, monomer, tail-to-tail	S26
A32	M1 + M5 = V1525 + FBR, non-covalent associate, core-to-core	S27
A41	M41 + M5 = V1179a + FBR, non-covalent associate, core-to-core	S28
A42	M42 + M5 = V1179b + FBR, non-covalent associate, core-to-core	S28

this case, a local temperature regime or overlapping of fragments ensures close contact and forms a covalent bond.

3. Conclusions

In conclusion, NDIs containing vinylbenzyl groups were synthesized via one-pot condensation followed by *O*-alkylation reaction. The new synthesized semiconductors are sufficiently thermally and electrochemically stable to meet the requirements for the application in photovoltaic devices. Owing to the presence of vinyl groups, all compounds are able to undergo thermal cross-linking during heating at 199°C and 213°C. All compounds have good E_{LUMO} alignment with the conduction band of the perovskite or Sb_2Se_3 light absorbers, while the E_{HOMO} energy levels are sufficiently high with reference to the valence band to block holes from the absorbers layer.

In neat films, cross-linking induces only minimal variations in electron mobility, indicating that the process does not cause significant molecular rearrangement. In contrast, donor–acceptor blends exhibit a marked improvement in electron mobility (by a factor of 2–3) after cross-linking, while maintaining stable hole transport. Importantly, cross-linking effectively suppresses the formation of deep traps over time, leading to significantly enhanced long-term operational stability. DSC and solubility testing identify a two-step cross-linking mechanism: a low-temperature linear polymerization followed by high-temperature three-dimensional network formation. Molecular modelling analysis reveals that steric factors, substituent orientation and blend composition dictate packing modes and cross-linking efficiency, with certain configurations promoting more ordered network formation. Taken together, these results establish vinylbenzyl-functionalized NDIs as promising n-type charge-transporting materials that combine efficient electron conduction, tuneable morphology and durable cross-linked networks.

Ethics. This work did not require ethical approval from a human subject or animal welfare committee.

Data accessibility. Supplementary material is available online [25]. All necessary information to reproduce experiments is described in this file, as well as additional supporting statements.

Declaration of AI use. We have not used AI-assisted technologies in creating this article.

Authors' contributions. L.M.S.: formal analysis, investigation, methodology; E.K.: investigation; A.J.: formal analysis, investigation; V.G.: data curation, formal analysis, resources; T.M.: formal analysis, validation; V.J.: conceptualization, project administration, supervision, writing—original draft, writing—review and editing; R.J.Č.: investigation; A.G.: investigation, software; K.G.: conceptualization, data curation, investigation, supervision, writing—original draft, writing—review and editing.

All authors gave final approval for publication and agreed to be held accountable for the work performed therein.

Conflict of interest declaration. We declare we have no competing interests.

Funding. This research was funded by a grant (No. S-MIP-22-8) from the Research Council of Lithuania. Computations were performed on resources at the High-Performance Computing Center 'HPC Saulėtekis' (Faculty of Physics, Vilnius University, Lithuania).

References

1. Zhang F. 2019 Dopant-free star-shaped hole-transport materials for efficient and stable perovskite solar cells. *J. Am. Chem. Soc.* **141**, 19700–19707. (doi:10.1021/jacs.9b08424)
2. He D, Zhao P, Feng Y, Zhang B. 2024 Low-temperature crosslinked hole transport material for high-performance inverted perovskite solar cells. *J. Chem. Eng.* **500**, 156886. (doi:10.1016/j.cej.2024.156886)
3. Wang L *et al*. 2021 A crosslinked polymer as dopant-free hole-transport material for efficient n-i-p type perovskite solar cells. *Journal of Energy Chemistry* **55**, 211–218. (doi:10.1016/j.jechem.2020.06.062)
4. Kamarauskas E *et al*. 2024 Cross-linkable fluorene-based hole transporting materials for perovskite solar cells. *Chem. Phys.* **579**, 112183. (doi:10.1016/j.chemphys.2024.112183)
5. Yang X, Luo X, Guo Y, Zhao D, Sheibani E, Xu B. 2024 Recent advances in cross-linkable organic hole-transporting materials for perovskite optoelectronics. *J. Mater. Chem. C.* **12**, 18952–18971. (doi:10.1039/D4TC04111A)
6. Wang Y *et al*. 2021 Cross-linked hole transport layers for high-efficiency perovskite tandem solar cells. *Sci. China Chem.* **64**, 2025–2034. (doi:10.1007/s11426-021-1059-1)
7. Vaitukaitytė D, Al-Ashouri A, Daškevičienė M, Kamarauskas E, Nekrasovas J, Jankauskas V, Magomedov A, Albrecht S, Getautis V. 2021 Enamine-based cross-linkable hole-transporting materials for perovskite solar cells. *Sol. RRL* **5**, 2000597. (doi:10.1002/solr.202000597)
8. Daskeviciute-Geguziene S, Magomedov A, Daskeviciene M, Genevicius K, Nekrasas N, Jankauskas V, Kantminiene K, McGehee MD, Getautis V. 2022 Cross-linkable carbazole-based hole transporting materials for perovskite solar cells. *Chem. Commun* 7495–7498. (doi:10.1039/D2CC02612K)
9. Vaitukaityte D, Magomedov A, Rakstys K, Kwiatkowski S, Kamarauskas E, Jankauskas V, Rousseau J, Getautis V. 2023 Thermally cross-linkable fluorene-based hole transporting materials: synthesis, characterization, and application in perovskite solar cells. *RSC Adv* **13**, 26933–26939. (doi:10.1039/D3RA04571C)
10. Kamarauskas E *et al*. 2024 Cross-linkable fluorene-based hole transporting materials for perovskite solar cells. *J. Chem. Phys.* **579**, 112183. (doi:10.1016/j.chemphys.2024.112183)
11. Daskeviciute-Geguziene S *et al*. 2024 In Situ Thermal Cross-Linking of 9,9′-Spirobifluorene-Based Hole-Transporting Layer for Perovskite Solar Cells. *ACS Appl. Mater. Interfaces* **16**, 1206–1216. (doi:10.1021/acsami.3c13950)
12. Li G, Zhu R, Yang Y. 2012 Polymer solar cells. *Nat. Photonics* **6**, 153–161. (doi:10.1038/nphoton.2012.11)
13. Zhao W, Li S, Yao H, Zhang S, Zhang Y, Yang B, Hou J. 2016 Molecular optimization enables over 13% efficiency in organic solar cells. *J. Am. Chem. Soc.* **138**, 9804–9813. (doi:10.1021/jacs.6b04991)
14. He Z, Zhong C, Su S, Xu M, Wu H, Cao Y. 2015 Enhanced power-conversion efficiency in polymer solar cells using an inverted device structure. *Nat. Photonics* **9**, 174–179. (doi:10.1038/nphoton.2015.6)
15. Li Y. 2020 Ternary organic solar cells: a review of recent advances. *Adv. Energy Mater.* **10**, 1902463. (doi:10.1002/aenm.201902463)
16. Wang H, Zhang C, Yao Y, Cheng C, Wang K. 2024 Non-fullerene organic electron transport materials toward stable and efficient inverted perovskite photovoltaics. *Small* **20**, 2403193. (doi:10.1002/smll.202403193)
17. Sun H *et al*. 2020 Side chain engineering of polymer acceptors for all-polymer solar cells with enhanced efficiency. *J. Mater. Chem. C.* **8**, 4012–4020. (doi:10.1039/D0TC00087F)
18. Jameel MA, Yang TCJ, Wilson GJ, Evans RA, Gupta A, Langford SJ. 2021 Naphthalene diimide-based electron transport materials for perovskite solar cells. *J. Mater. Chem. A.* **9**, 27170–27192. (doi:10.1039/D1TA08424K)
19. Svirskaite LM, Mandati S, Spalatu N, Malinauskiene V, Karazhanov S, Getautis V, Malinauskas T. 2022 Asymmetric NDI electron transporting SAM materials for application in photovoltaic devices. *Synth. Met.* **291**, 117214. (doi:10.1016/j.synthmet.2022.117214)
20. Connelly NG, Geiger WE. 1996 Chemical redox agents for organometallic chemistry. *Chem. Rev.* **96**, 877–910. (doi:10.1021/cr940053x)
21. Pavlishchuk VV, Addison AW. 2000 Conversion constants for redox potentials measured versus different reference electrodes in acetonitrile solutions at 25°C. *Inorg. Chim. Acta* **298**, 97–102. (doi:10.1016/S0020-1693(99)00407-7)

22. Magomedov A, Getautis V, Al-Ashouri A, Daškevičienė M, Vaitukaitytė D, Kamarauskas E, Jankauskas V, Rousseau J, Kwiatkowski S. 2023 Cross-linkable systems for organic and perovskite solar cells. *SSRN* **579**, 112183. (doi:10.2139/ssrn.4539058)
23. Baran D *et al*. 2016 Reduced voltage losses yield 10% efficient fullerene free organic solar cells with >1 V open circuit voltages. *Energy Environ. Sci.* **9**, 3783–3793. (doi:10.1039/c6ee02598f)
24. Frisch MJ *et al*, Gaussian 16, Revision C.01. 2016 Wallingford CT: Gaussian, Inc.
25. Svirskaite LM *et al*. 2026 Supplementary material from: Cross-Linkable Naphthalene Diimide Acceptors for Application in Photovoltaic Devices. Figshare. (doi:10.6084/m9.figshare.c.8449374)